



# Boosting electrocatalytic performance and durability of Pt nanoparticles by conductive $\text{MO}_{2-x}$ (M = Ti, Zr) supports

Wenjuan Shi<sup>a</sup>, Hyun-Uk Park<sup>b</sup>, Ah-Hyeon Park<sup>a</sup>, Liangyao Xue<sup>c</sup>, Seong-Kyu Kim<sup>a</sup>,  
Gu-Gon Park<sup>b</sup>, Young-Uk Kwon<sup>a,\*</sup>

<sup>a</sup> Department of Chemistry, Sungkyunkwan University, Suwon 16419, Republic of Korea

<sup>b</sup> Fuel Cell Laboratory, Korea Institute of Energy Research, Daejeon 34129, Republic of Korea

<sup>c</sup> State Key Laboratory of Molecular Engineering of Polymers, Department of Macromolecular Science, Fudan University, Shanghai 200438, China

## ARTICLE INFO

### Keywords:

Strong metal-support interaction

Conductive metal oxide

Durability

Oxygen reduction reaction

## ABSTRACT

Metal oxides, especially  $\text{TiO}_2$ , have been studied as an alternative support to replace the carbon in the conventional Pt/C catalysts for their high electrochemical stability at high electrode potentials. The low conductivity of metal oxides has been a big hurdle. In this work, we successfully overcome this issue by forming conductive  $\text{MO}_{2-x}$  (M = Ti and Zr) through solid state reduction with  $\text{NaBH}_4$ . The temperature of the reaction has turned out to be a crucial parameter to obtain highly conductive  $\text{MO}_{2-x}$ . Pt/ $\text{MO}_{2-x}$  catalysts were prepared by depositing Pt nanoparticles (NPs) on  $\text{MO}_{2-x}$  supports whose analysis data, show that the Pt NPs are uniformly deposited on the surface of  $\text{MO}_{2-x}$  supports and that there is a strong electronic interaction between Pt NPs and  $\text{MO}_{2-x}$  supports. The electrocatalysis of Pt/ $\text{MO}_{2-x}$  catalysts for oxygen reduction reaction (ORR) has been studied. Pt/ $\text{MO}_{2-x}$  catalysts show significantly enhanced mass activity (MA) and specific activity (SA) from those of Pt/C catalyst. More importantly, Pt/ $\text{MO}_{2-x}$  catalysts show a superior long-term durability. After 50,000 cycles of durability test, Pt/T370 catalyst retains 75%/84% of initial MA/SA, and Pt/Z438 catalyst retains 81%/88% of initial MA/SA, while Pt/C catalyst keeps only 36%/56% of initial MA/SA after 30,000 cycles. The significantly enhanced ORR performance of Pt/ $\text{MO}_{2-x}$  catalysts is attributed to the strong metal-support interaction (SMSI) effect between  $\text{MO}_{2-x}$  and Pt NPs as well as the high conductivity of  $\text{MO}_{2-x}$  supports. We believe Pt/ $\text{MO}_{2-x}$  catalysts are a promising form of electrocatalysts that can replace the presently dominating but not quite satisfactory Pt/C in fuel cell applications.

## 1. Introduction

Polymer electrolyte membrane fuel cells (PEMFCs) are a promising energy conversion system for their pollution-free process and high efficiency. For the large-scale commercialization of PEMFCs, highly active and durable catalysts for ORR are crucial. Thus far, the most common form of ORR catalysts is composed of Pt nanoparticles (NPs) dispersed on a porous carbon support, Pt/C [1–3]. Here, porous carbon materials are used for their large surface areas and high electrical conductivities. However, because of the weak metal-support interactions between carbon and Pt, agglomeration of Pt NPs occurs during long-term operation. In addition, carbon materials generally suffer from severe corrosion caused by the high potentials of the cell operation, resulting in accelerated loss of Pt surface area and worsened mass transport in the catalyst layer. These problems raise the issue of the low durability of

Pt/C catalysts [4–6].

Oxides of some metals have some desirable properties to be used as support materials such as high resistance to strongly corrosive stresses. Indeed, there are many cases in which metal oxide supports find successful applications when the conditions are demanding [7–11]. Furthermore, in some cases, metal oxides can interact with the supported metal NPs to alter their electronic structures [12–15], endowing them enhanced catalytic activity. For instance, Pt/ $\text{TiO}_2$  [16–18], Pd/ $\text{TiO}_2$  [19,20] and Pd/ $\text{Fe}_2\text{O}_3$  [21] catalysts have been reported to show enhanced catalytic activities from those of corresponding catalysts using carbon supports or without any support.

However, the low electrical conductivity of most of metal oxides have hindered the development of electrocatalysts using metal oxide supports. Efforts have been made to overcome this shortcoming of metal oxides, mostly by combining with carbon materials such as mixing metal

\* Corresponding author.

E-mail address: [ywkwon@skku.edu](mailto:ywkwon@skku.edu) (Y.-U. Kwon).

<https://doi.org/10.1016/j.apcatb.2023.122692>

Received 30 December 2022; Received in revised form 24 February 2023; Accepted 24 March 2023

Available online 25 March 2023

0926-3373/© 2023 Elsevier B.V. All rights reserved.

oxide NPs of 10–100 nm in size with porous carbon and depositing Pt or Pd NPs on it. Although the electrocatalysis by such a catalyst is enhanced compared with Pt/C, the enhancement is rather marginal. Further efforts such as utilizing a designed nanocomposite between metal oxide and a form of carbon as in  $\text{TiO}_2/\text{cup-stacked CNT}$  and  $\text{NbO}_x$  NPs embedded in the nanopores of porous carbon have been reported [22, 23]. However, as long as both metal oxide and carbon have available surfaces for metal NPs to deposit, direct contacts between metal NPs with carbon cannot be avoided completely and, hence, the problem of Pt–C contact is not fully alleviated.

A more fundamental approach would be to use a conductive metal oxide as the support. In the literature, there are numerous examples of treating metal oxides to endow electrical conductivity. For example, in case of  $\text{TiO}_2$ , doping of an aliovalent element on the cationic site or the anionic site or both has been reported to be an efficient method to reduce the band gap of  $\text{TiO}_2$ . In addition, creating oxygen vacancies to make  $\text{TiO}_{2-x}$  has been proven as a viable approach to increase the conductivity of  $\text{TiO}_2$  [24]. Toward this end, many different methods, such as treating  $\text{TiO}_2$  with a reducing agent, such as  $\text{NaBH}_4$  or  $\text{KBH}_4$  by solid-state reactions [25–27] at elevated temperatures or lithium-ethylene diamine at room temperature [28], and by electrochemical reduction [29,30], flame reaction [31], and even microwave [32] in addition to the conventional method of treating  $\text{TiO}_2$  with  $\text{H}_2$ , pure or mixed with  $\text{N}_2$  or Ar, at high temperatures. The resultant conductive  $\text{TiO}_2$  are reported to maintain the other beneficial properties of  $\text{TiO}_2$  practically intact [24,33], and thus has been widely applied in various fields of materials development such as catalysis [33,34], photocatalysis [35–37], and photoconducting materials [38,39]. Interestingly, however, there has been no report on using any of these conductive  $\text{TiO}_2$  as the support material for noble metal NPs for the electrocatalysis applications.

In addition to  $\text{TiO}_2$ ,  $\text{ZrO}_2$  appears to have many desirable properties as a support material for electrocatalysis. However, studies on endowing electrical conductivity to  $\text{ZrO}_2$  have been scarce probably because of the high stability and the large band gap of  $\text{ZrO}_2$ . Nevertheless, it may be rewarding if stable and conductive  $\text{ZrO}_{2-x}$  derivatives can be produced. In the literature, except for treating  $\text{ZrO}_2$  with a very high pressure  $\text{H}_2$ , there are very a few examples of  $\text{ZrO}_{2-x}$  in which  $\text{ZrO}_2$  was treated by rather unconventional methods such as electrolysis in a molten salt [40], reduction by molten Li [41], and even applying a high torsional force [42]. None of the aforementioned methods for  $\text{TiO}_{2-x}$  production appears to be effective in producing  $\text{ZrO}_{2-x}$ .

In this study, we prepared reduced  $\text{TiO}_2$  and  $\text{ZrO}_2$  by the solid-state reduction method by  $\text{NaBH}_4$  mentioned above and used them as the supports for Pt NPs and studied the resultant Pt/ $\text{TiO}_{2-x}$  and Pt/ $\text{ZrO}_{2-x}$  catalysts for ORR. We found that these catalysts showed significantly enhanced ORR activity over that of Pt/C. Furthermore, these catalysts show remarkably enhanced durability, far surpassing the 2025 DOE target (mass activity  $\leq 40\%$  loss of initial).

## 2. Experimental section

### 2.1. Materials

Titanium(IV) oxide ( $\text{TiO}_2$ ; 99.5%), Zirconium(IV) oxide ( $\text{ZrO}_2$ ; 99%), Chloroplatinic acid hexahydrate ( $\text{H}_2\text{PtCl}_6 \cdot 6 \text{H}_2\text{O}$ ; 37.5%), Sodium borohydride ( $\text{NaBH}_4$ ; 98%), Perchloric acid ( $\text{HClO}_4$ ; 70%) isopropyl alcohol (IPA; 99.7%) and a Nafion solution (5 wt%) were purchased from Aldrich. Commercial Pt/C (40 wt%) electrocatalyst was obtained from Johnson Matthey.  $\text{N}_2$  and  $\text{O}_2$  gases were purchased from the Deokyang Co. Filter papers (pore size: 0.45  $\mu\text{m}$ ) were purchased from Whatman. Ultrapure water (Genesys, 18 M $\Omega$  cm) was used throughout the work.

### 2.2. Synthesis of reduced $\text{MO}_{2-x}$ supports

0.1 mol of  $\text{MO}_2$  and 0.05 mol of  $\text{NaBH}_4$  were ground in together in a mortar and pestle for about 30 min. The mixture was placed in an alumina boat which, in turn, was placed in a tube furnace. The temperature was increased to a designated temperature between 300 and 450  $^\circ\text{C}$  with a heating rate of 10  $^\circ\text{C min}^{-1}$  under a  $\text{N}_2$  atmosphere, and kept at that temperature for 1 h. After cooling to room temperature, the sample was washed with water for several times in order to remove the residual  $\text{NaBH}_4$  and by-products. After filtration, the cake was dried in an oven at 80  $^\circ\text{C}$  for one day. Hereafter, these samples will be denoted as  $\text{MO}_{2-x}$  when referring to them collectively and as  $\text{TiO}_{2-x}$  and  $\text{ZrO}_{2-x}$  when referring to the individual groups separately. When referring to individual samples, those obtained from  $\text{TiO}_2$  will be denoted as T-temp and those from  $\text{ZrO}_2$  as Z-temp where temp stands for the heat-treatment temperature used to prepare  $\text{MO}_{2-x}$ .

### 2.3. Synthesis of Pt/ $\text{MO}_{2-x}$ catalysts

To synthesize Pt/ $\text{MO}_{2-x}$  catalysts, Pt NPs were formed in the presence of  $\text{MO}_{2-x}$  supports. 50 mg of  $\text{MO}_{2-x}$  was dispersed in 30 mL of water to get a suspension solution. To this solution, 1 mL of 0.1 M of  $\text{H}_2\text{PtCl}_6$  solution was added under vigorous stirring. After adding 5 mL of 0.1 M of  $\text{NaBH}_4$  solution, the mixture solution was stirred for 3 h at room temperature. The obtained catalyst was filtered, washed with water, and then dried. The catalysts will be denoted as Pt/ $\text{MO}_{2-x}$ , Pt/ $\text{TiO}_{2-x}$ , or Pt/ $\text{ZrO}_{2-x}$  when referring to them as a group or Pt/T-temp or Pt/Z-temp when referring to an individual sample.

### 2.4. Characterization

X-ray diffraction (XRD) patterns were obtained on a DC/MAX 2000 diffractometer, utilizing a Cu K $\alpha$  radiation ( $\lambda = 0.15406 \text{ nm}$ ) in  $2\theta = 10 \sim 90^\circ$ . Transmission electron microscopy (TEM) and high-resolution TEM (HR-TEM) images of catalysts were acquired in a JE-3011 microscope operated at 300 kV. High-angle annular dark field scanning transmission electron microscopy (HAADF-STEM) was carried out on a FEI Tecnai G2 F30 TEM operating at 200 kV. Raman spectra were recorded by using a WITTEC Raman spectrometer in the range of 100  $\sim$  800  $\text{cm}^{-1}$  with 532 nm excitation. X-ray photoelectron spectroscopy (XPS) experiments were performed using an ESCA 2000 instrument with a monochromatic Al K $\alpha$  X-ray source. The binding energies were calibrated by C 1 s peak at 284.6 eV. The contents of Pt in the Pt/ $\text{MO}_{2-x}$  catalysts were determined by inductively coupled plasma atomic emission spectroscopy (ICP-AES, OPTIMA 4300DV Perkin Elmer). Thermogravimetric (TG) analysis was performed on a STA7200 (HITACHI) instrument in air. The conductivity of samples was measured by the standard four-probe method at room temperature. The ex-situ hard X-ray Absorption spectroscopy (XAS) measurements of Ti K-edge and Zr K-edge were carried out at the 1W1B beamline of the Beijing Synchrotron Radiation Facility (BSRF). The ex-situ Ti K-edge and Zr K-edge absorption fine structure (XAFS) data were acquired with transmission mode.  $E_0$  of the standard foil was assigned by the first maximum of the first-derivative X-ray absorption near-edge structures (XANES) spectrum. All data were aligned according to the standard foil. The XAFS raw data were calibrated and normalized by the ATHENA program.

### 2.5. Electrochemical measurements

All electrochemical experiments were performed with a conventional three-electrode electrochemical workstation which were assembled to a potentiostat (Ivium Compactstat, Ivium technology). The working electrode was a glassy carbon rotating disk electrode (RDE) with a diameter of 5 mm. A Pt wire was used as the counter electrode and a standard Ag/AgCl (sat'd with KCl) electrode as the reference electrode. To make a working electrode, a catalyst powder was dispersed

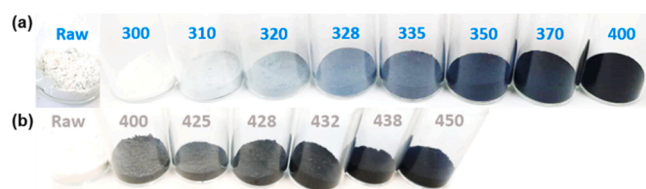


**Fig. 1.** Photographs of (a) raw  $\text{TiO}_2$  and  $\text{TiO}_{2-x}$  and (b) raw  $\text{ZrO}_2$  and  $\text{ZrO}_{2-x}$  supports. The onset temperature of the color change of  $\text{ZrO}_2$  is 400 °C, 80 °C higher than that of  $\text{TiO}_2$ , which probably is because of the higher stability of  $\text{ZrO}_2$  than  $\text{TiO}_2$ .

in 2.5 mL of a mixed solution of deionized water and IPA ( $v/v = 4:1$ ), and 10  $\mu\text{L}$  of liquid Nafion (5% solution) under ultrasonication to obtain a well-dispersed suspension. 1 ~ 3  $\mu\text{L}$  of the suspension was pipetted onto the RDE electrode and dried to make the catalyst loading to be 20  $\mu\text{g cm}^{-2}$ . Cyclic voltammetry (CV) was carried out at a scan rate of 20  $\text{mV s}^{-1}$  in 0.1 M  $\text{HClO}_4$  aqueous solution with  $\text{N}_2$  purging. The electrochemical surface area (ECSA) was calculated from the hydrogen desorption charge after a double-layer current correction with an assumed value of 210  $\mu\text{C cm}^{-2}$  on the Pt surface by the relation:  $\text{ECSA} = \frac{Q_H}{m \cdot q_H}$  where  $Q_H$  is the charge for hydrogen desorption,  $m$  is the amount of metal (Pt) in the catalyst, and  $q_H$  is the value of charge required for the desorption of a monolayer of hydrogen on the Pt surface. The ORR polarization curves were recorded in  $\text{O}_2$ -saturated 0.1 M  $\text{HClO}_4$  solution at the scan rate of 10  $\text{mV s}^{-1}$  with the rotating speed of 1600 rpm. The durability of the catalysts was tested following the protocol of accelerated stress test (AST) which is constituted of successive chronoamperometry cycles at 0.6 V for 3 s and 0.95 V for 3 s in an  $\text{N}_2$ -saturated aqueous 0.1 M  $\text{HClO}_4$  solution. Up to 50,000 cycles were tried for our catalysts. For comparison of all measurements, a commercial Pt/C catalyst (40 wt%) was also tested under the same conditions.

## 2.6. Membrane electrode assembly (MEA) and testing

Commercially available carbon-coated gas diffusion layer (GDL SIGRACET 35 BCE) was used as the catalyst support for all fuel cell experiments. The cathode catalyst ink was mixed with Nafion (5% solution), water and isopropanol, then sonicated for 2 h to achieve homogeneous dispersion. The catalyst ink was then spread onto a GDL. The loading of anode and cathode catalyst was 0.15  $\text{mg}_{\text{Pt}} \text{cm}^{-2}$ . The anode and cathode electrodes were hot-pressed onto a Nafion 212 membrane at 130 °C and 1.0 MPa for 3 min. The resulting MEA was cooled and then assembled in a 5  $\text{cm}^2$  single cell for testing. The  $\text{H}_2$  and air fuel oxidant gases were fully humidified and fed at flow rates of 200 sccm for  $\text{H}_2$  and 800 sccm for air under ambient pressure. To study the degradation/dissolution of the catalyst, AST protocol was employed. The protocol involved cycling the cathode potential in a rectangular waveform between 0.60 and 0.95 V with 3 s of holding time at each potential for 30,000 cycles and mimicked no-load to full-load transitions during fuel cell operation.

## 3. Results and discussion

The Pt/ $\text{MO}_{2-x}$  catalysts in this study were obtained in two-steps:  $\text{MO}_{2-x}$  supports were synthesized by a solid-state reduction with  $\text{NaBH}_4$  at different temperatures, followed by the deposition of Pt NPs on  $\text{MO}_{2-x}$  supports. Here we will discuss the  $\text{MO}_{2-x}$  supports first and then proceed to Pt/ $\text{MO}_{2-x}$  catalysts.

### 3.1. Synthesis and characterization of $\text{MO}_{2-x}$ Supports

The reactions of  $\text{MO}_2$  with  $\text{NaBH}_4$  resulted in variously colored products depending on the nature of  $\text{MO}_2$  and the heat-treatment temperature (Fig. 1). The color of  $\text{TiO}_{2-x}$  samples changes from white of raw

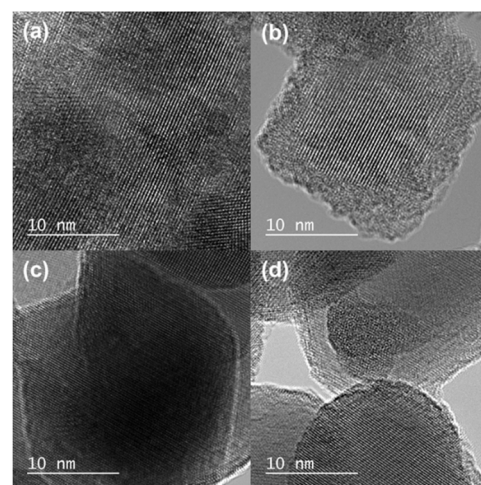


**Fig. 2.** HRTEM images of (a) raw  $\text{TiO}_2$ , (b) T-370, (c) raw  $\text{ZrO}_2$  and (d) Z-438.

$\text{TiO}_2$  to light steel blue, light blue, steel blue and dark blue, and the color of  $\text{ZrO}_{2-x}$  samples changes from white of raw  $\text{ZrO}_2$  to light gray, deep gray and dark gray as the heat-treatment temperature increases. The higher the reduction temperature is, the deeper the color of  $\text{MO}_{2-x}$  becomes. These color changes agree well with those of corresponding  $\text{MO}_{2-x}$  obtained by other reduction methods of  $\text{MO}_2$  in the literature [43], in which the colors are attributed to the formation of oxygen defects and accompanying reduction of  $\text{M}^{4+}$  ions to  $\text{M}^{3+}$  ions. The various colors of our  $\text{MO}_{2-x}$  samples suggest the easy control of the defect concentration by our method.

The crystalline states of  $\text{MO}_{2-x}$  samples were characterized by XRD (Fig. S1). The patterns of  $\text{TiO}_{2-x}$  show peaks of anatase and rutile phases and those of  $\text{ZrO}_{2-x}$  show peaks of monoclinic and tetragonal phases of  $\text{ZrO}_2$ . Compared with raw  $\text{TiO}_2$ , the patterns of  $\text{TiO}_{2-x}$  show that the peaks of anatase phase are decreased in intensity as the heat-treatment temperature increases while those of rutile phase do not change as much. Likewise, the peaks of the monoclinic phase of  $\text{ZrO}_{2-x}$  are decreased in intensity with temperature while those of the tetragonal phase are more or less intact. These observations suggest that the reduction occurs preferentially on anatase phase of  $\text{TiO}_2$  and on the monoclinic phase of  $\text{ZrO}_2$ , disrupting these lattices. Similar selective reduction of anatase phase has been reported [44,45], which probably is because of the different stabilities between the two phases of  $\text{TiO}_2$ . In case of  $\text{ZrO}_2$ , it is well-known that the tetragonal phase is more stable than the monoclinic phase when there is a certain amount of cationic and/or anionic defects [45,46].

The TEM images of  $\text{MO}_{2-x}$  samples (Figs. S2 and S3) show that the particle morphologies are not changed upon reduction. The average particle sizes, estimated from the histograms (Figs. S4 and S5), however, show that the particle size decreases, although slightly, with the heat-treatment temperature. In case of  $\text{TiO}_{2-x}$ , the average particle sizes are the largest for T-328 with 20.2 nm and the smallest for T-400 with 18.8 nm, which are all smaller than that of raw  $\text{TiO}_2$  (21.9 nm). Similarly, Z-450 shows the smallest particles with the average value of 27.1 nm and Z-400 the largest with 29.1 nm among  $\text{ZrO}_{2-x}$  samples, which are smaller than that of raw  $\text{ZrO}_2$  (32.3 nm). The decrease of the particle size can be explained with the increase of the oxygen defect concentration with the heat-treatment temperature.

The HRTEM images of T-370 and Z-438 supports (determined to be the optimal ones from the respective groups; see below) along with those of raw  $\text{MO}_2$  are shown in Fig. 2. While the images of raw  $\text{MO}_2$  show well developed lattice fringes on the entire particles, those of  $\text{MO}_{2-x}$  show some defects and irregular lattice fringes concentrated on the surfaces of the particles. The latter observation suggests that the reduction reaction has occurred on the surfaces of the  $\text{MO}_2$  particles. Corresponding images

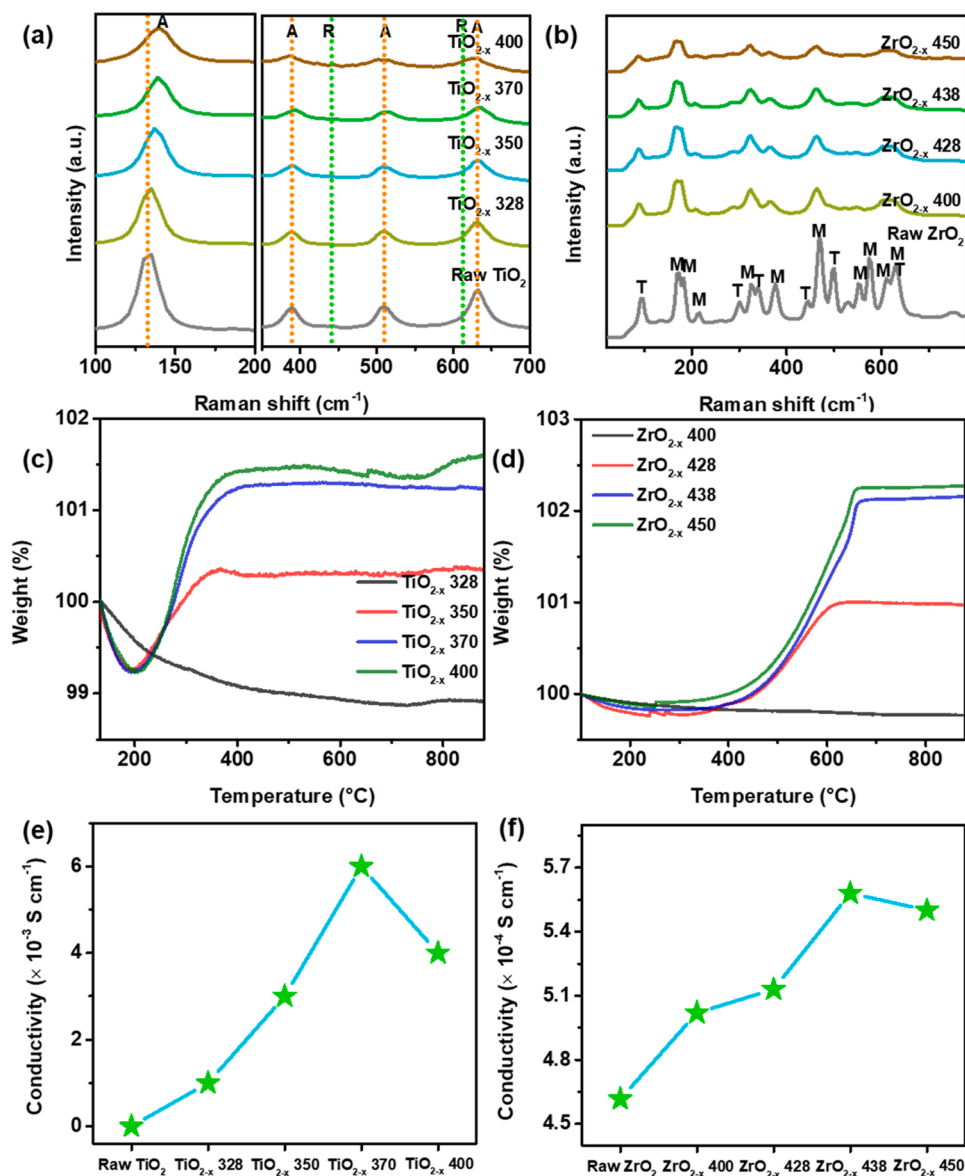


**Fig. 3.** Raman spectra of (a)  $\text{TiO}_{2-x}$  and (b)  $\text{ZrO}_{2-x}$  supports. TG curves of (c)  $\text{TiO}_{2-x}$  and (d)  $\text{ZrO}_{2-x}$  supports. The conductivity curves of (e)  $\text{TiO}_{2-x}$  and (f)  $\text{ZrO}_{2-x}$  supports.

of other  $\text{MO}_{2-x}$  supports (Fig. S6) show that the defect concentration of the portion of the irregularity of lattice fringe increases with the heat-treatment temperature.

The selective changes between the two phases in each  $\text{MO}_{2-x}$  group, observed in the XRD patterns are also observed in their Raman spectra. In the Raman spectrum of raw  $\text{TiO}_2$  (Fig. 3a), the peaks at 144, 197, 399, 515, 519 and  $639 \text{ cm}^{-1}$  are assigned to the anatase phase [47–50]. These peaks become gradually weaker and broader as the heat-treatment temperature increases. Also, the peak at  $144 \text{ cm}^{-1}$  shows a gradual red-shift. These changes indicate the decrease of crystallinity of anatase in  $\text{TiO}_{2-x}$ , consistent with the XRD results. The peaks of the rutile phase at 447 and  $612 \text{ cm}^{-1}$  are much weaker because of its smaller content in the sample as seen in its XRD pattern, prohibiting any deeper analysis. In Fig. 3b, the Raman spectra of  $\text{ZrO}_{2-x}$  are significantly changed compared with that of raw  $\text{ZrO}_2$ . The peaks of the monoclinic phase are broadened and their intensities are considerably decreased. On the contrary, the tetragonal phase does not show much change although the peaks are very weak prohibiting any detailed analysis.

The amounts of oxygen defects of  $\text{MO}_{2-x}$  samples were estimated from their TG data in air (Fig. 3c and d). After the loss of adsorbed water

below  $200 ^{\circ}\text{C}$ , both  $\text{TiO}_2$  and  $\text{ZrO}_2$  continue to lose some additional weights which can be attributed to the loss of surface -OH groups. By contrast, all  $\text{MO}_{2-x}$  samples gain weights after the water losses.  $\text{TiO}_{2-x}$  samples gain weights up to about  $390 ^{\circ}\text{C}$  and do not show any change. Similarly,  $\text{ZrO}_{2-x}$  samples gain weights up to about  $660 ^{\circ}\text{C}$  and do not show any further change. The differences of the residual weights between  $\text{MO}_{2-x}$  and corresponding  $\text{MO}_2$  are attributed to the amounts of oxygen defects in  $\text{MO}_{2-x}$ , by which the x-values are calculated to be  $0.03 - 0.12$  for  $\text{TiO}_{2-x}$  and  $0.08 - 0.15$  for  $\text{ZrO}_{2-x}$ . The highest x-values are from the samples with the highest heat-treatment temperatures. Reduction endows  $\text{MO}_{2-x}$  samples electrical conductivity (Fig. 3e and f). Raw  $\text{TiO}_2$  is a poor electrical conductor with the room temperature conductivity from four probe measurement of  $8.4 \times 10^{-7} \text{ S cm}^{-1}$ . The conductivity increases dramatically to  $1 \times 10^{-3} \text{ S cm}^{-1}$  for T-328 and to  $6 \times 10^{-3} \text{ S cm}^{-1}$  for T-370. Interestingly, the conductivity of T-400,  $4 \times 10^{-3} \text{ S cm}^{-1}$ , is lower than that of T-370, which probably is because of too excessive defects in this sample disrupting the lattice structure.  $\text{ZrO}_{2-x}$  samples are also conductors, but not as good as  $\text{TiO}_{2-x}$ , with the conductivity ranging from  $5.02 \times 10^{-4} \text{ S cm}^{-1}$  for Z-400– $5.58 \times 10^{-4} \text{ S cm}^{-1}$  for Z-438. Again, the sample with the highest heat-treatment



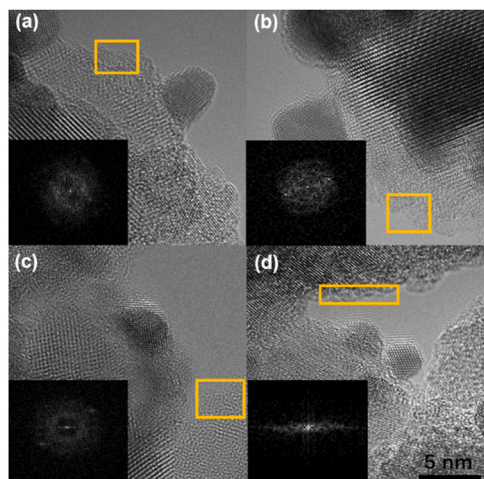


Fig. 4. TEM images of Pt/T328 (a), Pt/T350 (b), Pt/T370 (c) and Pt/T400 (d) catalysts. Inset FFT images on the regions marked by yellow boxes.

temperature, Z-450, is slightly less conductive with  $5.50 \times 10^{-4} \text{ S cm}^{-1}$  than Z-438. Based on these observations, one can conclude that there is an optimal temperature to endow conductivity to  $\text{MO}_{2-x}$ . In our case, it is about 370 °C for  $\text{TiO}_{2-x}$  and 438 °C for  $\text{ZrO}_{2-x}$ .

### 3.2. Synthesis and characterization of Pt/ $\text{MO}_{2-x}$ catalysts

Pt/ $\text{MO}_{2-x}$  catalysts were obtained by depositing Pt NPs on  $\text{MO}_{2-x}$  supports. Their XRD patterns show the peaks of Pt and  $\text{MO}_{2-x}$  (Fig. S7) without any extra peaks. The Pt peak positions were fitted by the least-squares method to calculate the lattice parameter of  $a = 3.90 \text{ \AA}$  for all Pt/ $\text{TiO}_{2-x}$  and  $3.89 \text{ \AA}$  for all Pt/ $\text{ZrO}_{2-x}$ . These values are slightly smaller than that of Pt in Pt/C,  $3.94(2) \text{ \AA}$ , suggesting lattice contractions. The crystallite sizes of Pt NPs were estimated from the width of the Pt(111) peaks. The size of Pt NPs gradually decreases from 5.5 nm for Pt/T328 to 4.9 nm for Pt/T400. Similarly, Pt NPs in Pt/ $\text{ZrO}_{2-x}$  decrease in size from 5.1 nm for Pt/Z400 to 4.5 nm for Pt/Z438. This observation appears to be related with the surface defect density. That is, the higher the heat-treatment temperature is, the higher defect density becomes, which, in turn, makes the nucleation rate of Pt NPs more facilitated, resulting in smaller Pt NPs. Therefore, between  $\text{TiO}_{2-x}$  and  $\text{ZrO}_{2-x}$ , the latter is more favorable for the nucleation of Pt NPs, probably because of the higher temperatures used to obtain them than the former. In addition, there may be some inherent factors associated with the nature of  $\text{ZrO}_2$  and  $\text{TiO}_2$  that may contribute to the different nucleation rates on them, which, however, is not possible to analyze at the present state. The Pt contents, determined by ICP elemental analyses, of these catalysts show that Pt/ $\text{ZrO}_{2-x}$  catalysts are 26.7 – 27.3%, slightly but not negligibly higher than 24.8 – 25.9% of Pt/ $\text{TiO}_{2-x}$  catalysts, consistent with the above assumed more favorable nucleation on  $\text{ZrO}_{2-x}$  than on  $\text{TiO}_{2-x}$ . In line with the facilitating role of the defects for the Pt NP nucleation, the Pt content increases as the heat-treatment temperature increases and those on  $\text{MO}_{2-x}$  are higher than those on raw  $\text{MO}_2$  supports are considerably smaller than their reduced counterparts (Table S1).

Uniform deposition of Pt NPs on the support is crucial for the performance and stability of the catalyst. The TEM images of Pt/ $\text{MO}_{2-x}$  show that the Pt NPs are well-dispersed on the  $\text{MO}_{2-x}$  surfaces although a few of Pt NPs are aggregated (Figs. S8–S11). Compared with conventional carbon supports, the hydrophilic  $\text{MO}_{2-x}$  NPs surfaces are expected will be more favorable for water absorption, which may contribute to the uniform distribution of the Pt NPs. The shape and size of  $\text{MO}_{2-x}$  NPs are practically unchanged from those before the deposition of Pt NPs. The sizes of Pt NPs were calculated statistically by measuring about 100 different Pt NPs in each sample. The average sizes range from 5.0 nm for Pt/T328 to 4.6 nm for Pt/T400, and from 4.9 nm for Pt/Z400 to 4.4 nm

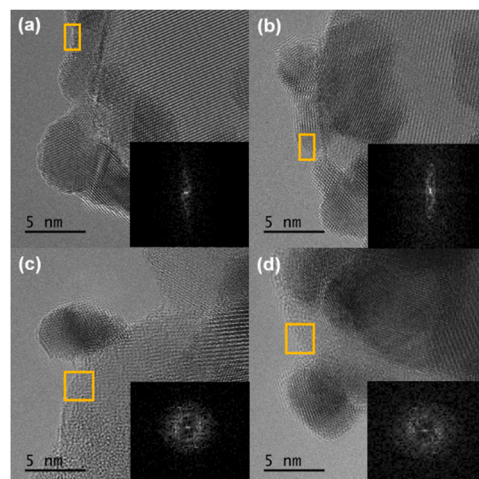


Fig. 5. TEM images of Pt/Z400 (a), Pt/Z428 (b), Pt/Z438 (c) and Pt/Z450 (d) catalysts. Inset FFT images on the regions marked by yellow boxes.

for Pt/Z450. These sizes and trends within each group are in good agreement with those estimated from the XRD data. The average size of Pt NPs in Pt/C is 3.7 nm, smaller than those of Pt/ $\text{MO}_{2-x}$  (Fig. S24).

We also examined Pt/ $\text{MO}_{2-x}$  samples with HRTEM and EDS mapping (Figs. S12–S19). On one hand, they confirm the observations from TEM that the Pt NPs are evenly deposited on  $\text{MO}_{2-x}$  supports. On the other hand, however, as shown in Figs. 4 and 5 for Pt/T370 and Pt/Z438, respectively, as the representative samples, the HRTEM images show irregular lattices on the rims of  $\text{MO}_{2-x}$  NPs. FFT images taken on those parts produced no pattern, indicating the presence of amorphous phases. The presence of amorphous phase on the outer part of each  $\text{MO}_{2-x}$  NPs suggests that the reduction of  $\text{MO}_2$  in our method takes place at the interfaces between  $\text{MO}_2$  particles and  $\text{NaBH}_4$ .

The XPS spectra of Pt/ $\text{TiO}_{2-x}$  and Pt/ $\text{ZrO}_{2-x}$  catalysts are shown in Figs. 6 and 7, respectively, along with those of reference  $\text{MO}_2$  and Pt/C. Numerical data from the XPS spectra are summarized in Tables S2–S7. The O 1s spectra (Figs. 6a and 7a) can be deconvoluted into three peaks at 529.85, 531.52, and 532.73 eV that are assigned to lattice oxygen atoms in  $\text{M}^{4+}\text{-O}$  and  $\text{M}^{3+}\text{-O}$  bonds, and OH<sup>−</sup> group, respectively [51–53]. The fraction of  $\text{M}^{4+}\text{-O}$  is 85.3 – 59.5% for Pt/ $\text{TiO}_{2-x}$  catalysts and 93.6 – 52.7% for Pt/ $\text{ZrO}_{2-x}$ , which are lower than 94.7% for raw  $\text{TiO}_2$  and 93.6% for raw  $\text{ZrO}_2$ . Within each Pt/ $\text{MO}_{2-x}$  series, the fraction of  $\text{M}^{4+}\text{-O}$  decreases monotonously as the heat-treatment temperature increases. Concurrently, the fraction of  $\text{M}^{3+}\text{-O}$  increases from 8.8% for Pt/T328 to 28.9% for Pt/T400 and from 10.1% for Pt/Z400 to 37.4% for Pt/Z450. In the Ti 2p spectra on Pt/ $\text{TiO}_{2-x}$  catalysts (Fig. 6b), the peaks of raw  $\text{TiO}_2$  at 458.75 and 464.59 eV are assigned to Ti 2p<sub>3/2</sub> and Ti 2p<sub>1/2</sub> of  $\text{Ti}^{4+}$  species [54,55], respectively. These peaks are down-shifted in Pt/ $\text{TiO}_{2-x}$  catalysts and the magnitude of shift increases with the heat-treatment temperature, further supporting that the  $\text{Ti}^{3+}$  content increases with temperature. The oxygen vacancy content, calculated from the relative peak intensities between  $\text{Ti}^{3+}$  and  $\text{Ti}^{4+}$ , monotonously increases with the heat-treatment with the lowest value of 8.8% for Pt/T328 and the highest of 32.7% for Pt/T400. Similarly, in the Zr 3d spectra on Pt/ $\text{ZrO}_{2-x}$  catalysts (Fig. 7b), the peaks of raw  $\text{ZrO}_2$  at 181.88 and 184.23 eV, assigned to Zr 3d<sub>5/2</sub> and Zr 3d<sub>3/2</sub> of  $\text{Zr}^{4+}$  species [56] are down-shifted to 181.85 and 184.20 eV for Pt/Z400 and further down-shifted monotonously with temperature to 181.65 and 183.99 eV for Pt/Z450, which indicate the presence of  $\text{Zr}^{3+}$  species in  $\text{ZrO}_{2-x}$  supports and the increase of its proportion with the heat-treatment temperature. Again, the oxygen vacancy content increases monotonously from 10.1% for Pt/Z400 to 37.4% for Pt/Z450. In addition to the formation of oxygen defects, the SMSI with Pt NPs may further increase the proportion of  $\text{M}^{3+}$ . In many cases in which SMSI effect is observed,

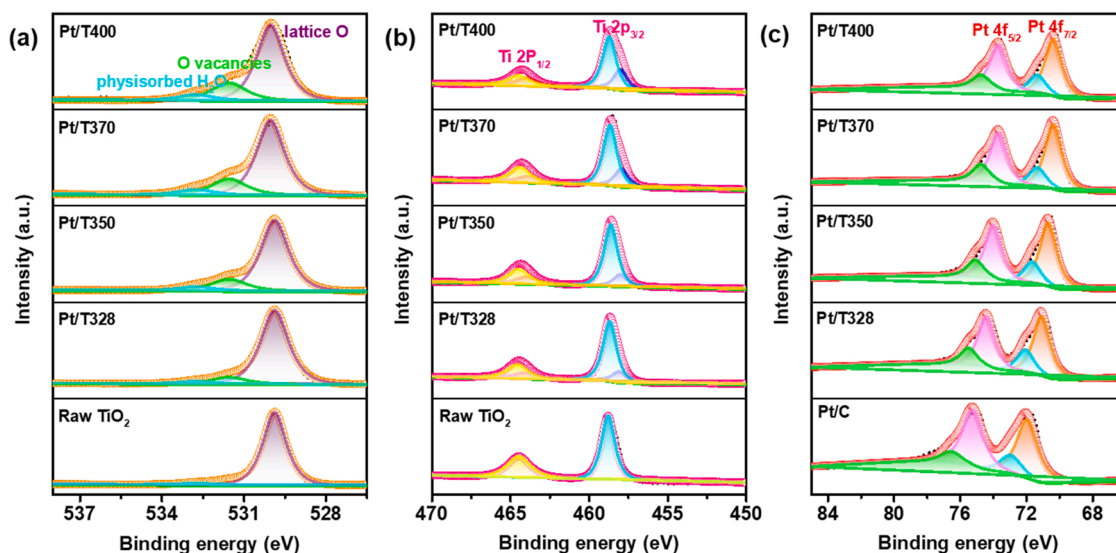


Fig. 6. XPS spectra of raw  $\text{TiO}_2$  and  $\text{Pt/TiO}_{2-x}$  and  $\text{Pt/C}$  catalysts: (a) O 1s, (b) Ti 2p and (c) Pt 4f.

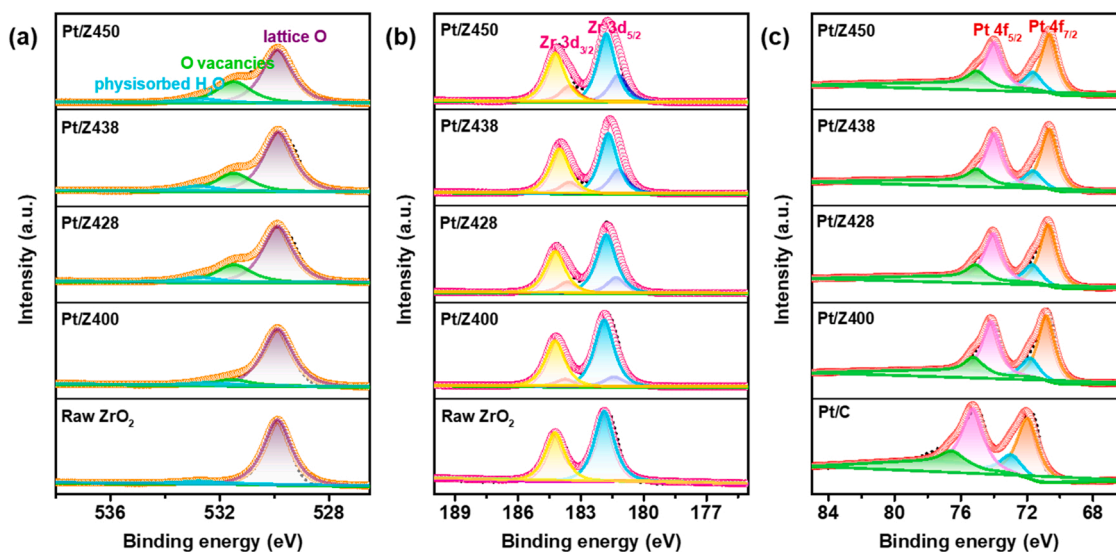


Fig. 7. XPS spectra of raw  $\text{ZrO}_2$  and  $\text{Pt/ZrO}_{2-x}$  and  $\text{Pt/C}$  catalysts: (a) O 1s, (b) Zr 3d and (c) Pt 4f.

noble metal atoms are directly bonded to the metal ions in metal oxide supports, inducing the partial reduction of the latter [57–61].

The Pt 4f spectra of  $\text{Pt/MO}_{2-x}$  are deconvoluted into 4  $f_{7/2}$  and 4  $f_{5/2}$  peaks of  $\text{Pt}^0$  and  $\text{Pt}^{2+}$  species (Figs. 6c and 7c). Because the two sets of peaks show the same trend of change, we will use  $\text{Pt}^0$  as the representative in the discussion of the trend of Pt 4f XPS. In  $\text{Pt/C}$  reference, the strong  $\text{Pt}^0$  peaks are located at 71.80 and 75.20 eV for Pt 4  $f_{7/2}$  and Pt 4  $f_{5/2}$ . These peaks show large down-shifts in both  $\text{Pt/MO}_{2-x}$  catalysts and the magnitudes increase with the heat-treatment temperature, indicating that SMSI is operative in these catalysts and the extent of SMSI varies within the series. In case of  $\text{Pt/TiO}_{2-x}$ , the largest shifts are observed in  $\text{Pt/T370}$  and  $\text{Pt/T400}$  with the two peaks appearing at 70.58 and 73.64 eV, respectively. The corresponding ones in  $\text{Pt/ZrO}_{2-x}$  are  $\text{Pt/Z438}$  and  $\text{Pt/Z450}$  with the peaks at 70.58 and 73.92 eV, respectively. The decrease of the binding energies of Pt XPS means the lowering of the Pt d-band center with respect to the Fermi level. According to the d-band center shift theory, this change brings in the reduction of the adsorption energy of reaction intermediates on the Pt surface increasing its catalytic activity [8,62,63].

In order to investigate the valence states M atoms in  $\text{Pt/MO}_{2-x}$

catalysts in details, we measured Ti K-edge and Zr K-edge XANES of  $\text{Pt/T370}$  and  $\text{Pt/Z438}$  samples, respectively, along with appropriate references (Fig. S20). All of the analysis data of the spectra indicate that the valence state of M atom is between +3 and +4 in these samples (See Supporting Information for details of XANES analyses.). In addition, the data on  $\text{Pt/T370}$  sample suggest severely disordered Ti–O coordination environment with five coordinated Ti atoms, suggesting the formation of  $\text{O}_v - \text{Ti}^{3+}$  species in this sample. The strong metal-support interaction can occur at the interface accompanied with the electron transfer from  $\text{O}_v - \text{Ti}^{3+}$  species to the adjacent interfacial Pt atoms to form  $\text{Pt}^{\delta-}$  sites. Therefore, abundant  $\text{Pt}^{\delta-}/\text{TiO}_{2-x}$  interfacial sites can be efficiently fabricated and stabilized over the  $\text{Pt/T370}$  catalyst.

In order to estimate the effect of the  $\text{MO}_{2-x}$  supports on the electronic structure of Pt NPs, we performed DFT calculations on model structures composed of a Pt block placed on top of a  $\text{TiO}_2$  or  $\text{TiO}_{2-x}$  block. The calculation results show that the electronic structure of Pt can be affected by simply bringing the Pt block in contact with the  $\text{TiO}_2$  or  $\text{TiO}_{2-x}$  block, not even inducing any chemical bond between them. Notably, the d-band center of Pt is lowered as the distance between Pt and  $\text{TiO}_2$  or  $\text{TiO}_{2-x}$  blocks become shorter, suggesting a kind of field

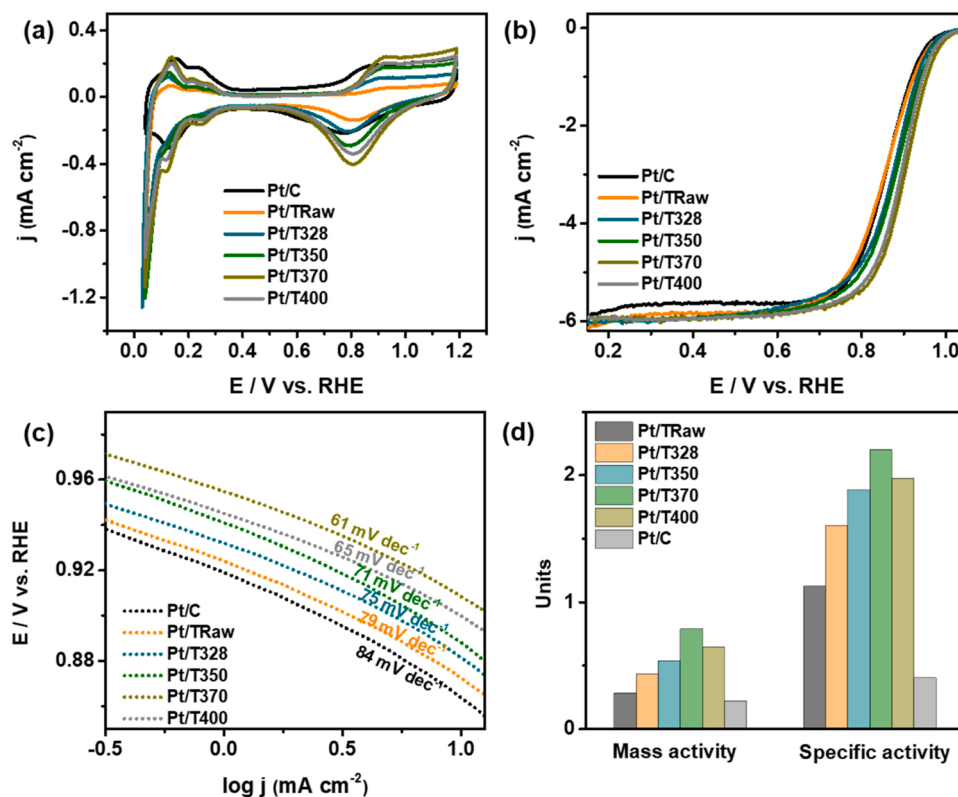


Fig. 8. Electrochemical analysis of Pt/TiO<sub>2-x</sub> and Pt/C catalysts in 0.1 M HClO<sub>4</sub>: (a) CVs (N<sub>2</sub> saturated, scan rate: 20 mV s<sup>-1</sup>), (b) LSVs for ORR (O<sub>2</sub> saturated, scan rate: 10 mV s<sup>-1</sup>), (c) Tafel plots, (d) normalized mass and specific activity at 0.9 V.

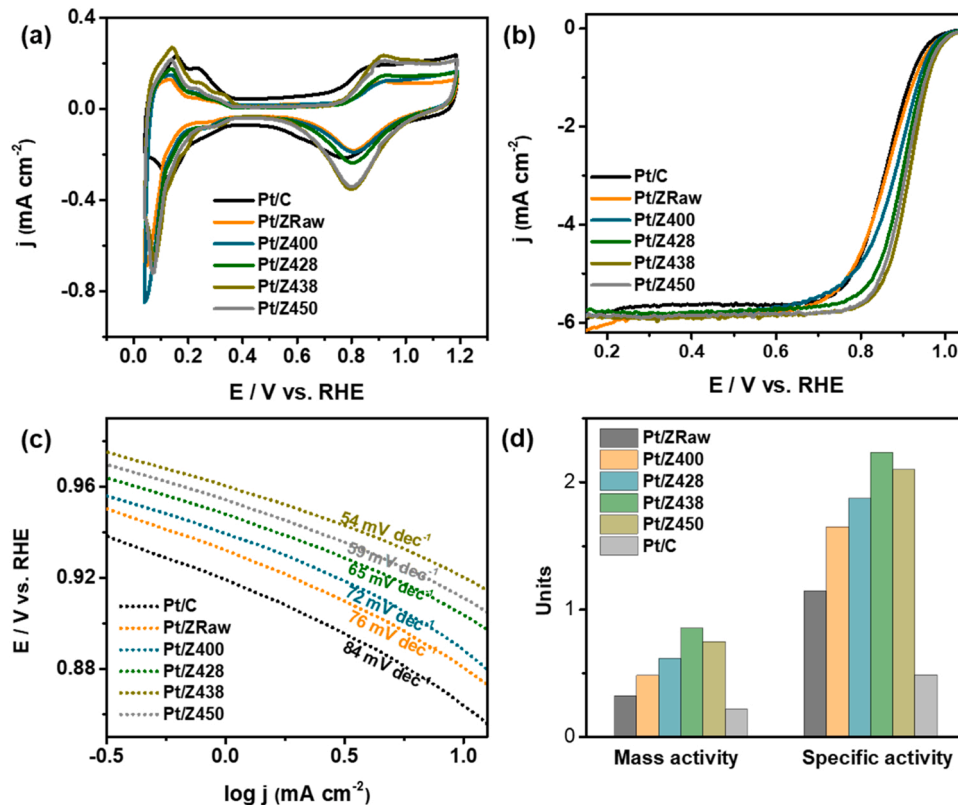


Fig. 9. Electrochemical analysis of Pt/ZrO<sub>2-x</sub> and Pt/C catalysts in 0.1 M HClO<sub>4</sub>: (a) CVs (N<sub>2</sub> saturated, scan rate: 20 mV s<sup>-1</sup>), (b) LSVs for ORR (O<sub>2</sub> saturated, scan rate: 10 mV s<sup>-1</sup>), (c) Tafel plots, (d) normalized mass and specific activity at 0.9 V.



**Table 1**ECSAs and LSV data of Pt/MO<sub>2-x</sub> and Pt/C catalysts for ORR.

Samples	ECSA (m <sup>2</sup> g <sub>Pt</sub> <sup>-1</sup> )	Mass activity (A mg <sub>Pt</sub> <sup>-1</sup> )	Specific activity (mA cm <sup>-2</sup> )	Half-wave potential (V)	Onset potential (V)
Pt/TRaw	24.68	0.277	1.122	0.857	0.927
Pt/T328	26.92	0.431	1.601	0.872	0.931
Pt/T350	28.38	0.534	1.881	0.879	0.939
Pt/T370	35.71	0.786	2.201	0.898	0.956
Pt/T400	32.67	0.645	1.974	0.893	0.945
Pt/ZRaw	27.92	0.319	1.142	0.865	0.931
Pt/Z400	29.12	0.479	1.645	0.879	0.939
Pt/Z428	32.88	0.615	1.870	0.895	0.945
Pt/Z438	38.50	0.852	2.213	0.914	0.958
Pt/Z450	35.56	0.745	2.095	0.904	0.953
Pt/C	44.70	0.216	0.483	0.853	0.921

effect on the electronic structure of Pt. The down-shifts of Pt 4 f XPS peaks in Pt/MO<sub>2-x</sub> compared with those of Pt/C may be caused by this effect (See [Supporting Information](#) for details of DFT calculations).

### 3.3. Electrochemical performance of oxygen reduction reaction

Pt/MO<sub>2-x</sub> catalysts were analyzed electrochemically. In addition to the Pt/MO<sub>2-x</sub> catalysts mentioned so far, Pt NPs were deposited on unreduced MO<sub>2</sub> to obtain Pt/T-raw and Pt/Z-raw catalysts and their data are included. The CVs are shown in [Figs. 8a and 9a](#). Typical peaks of Pt-based catalysts are observed. From the hydrogen desorption peaks at 0 ~ 0.35 V in the positive sweeps, the ECSAs were calculated to be in the range of 24.68 – 35.71 m<sup>2</sup> g<sub>Pt</sub><sup>-1</sup> for Pt/TiO<sub>2-x</sub> catalysts and 27.92 –

35.56 m<sup>2</sup> g<sub>Pt</sub><sup>-1</sup> for Pt/ZrO<sub>2-x</sub> catalysts. The general trends of the ECSA of the two groups are the same that it increases with the heat-treatment temperature within each group, but with one exception that the highest ECSA in Pt/TiO<sub>2-x</sub> is observed in Pt/T370, seconded by Pt/T400 ([Table 1](#)). The general trend of ECSA, therefore, appears to be determined mainly by the average size of the Pt NPs but other factors such as the electronic structure of Pt resulted from the interaction with MO<sub>2-x</sub> support may affect ECSA to some extent. The ECSAs of Pt/MO<sub>2-x</sub> catalysts are much smaller than that of the reference Pt/C, 44.70 m<sup>2</sup> g<sub>Pt</sub><sup>-1</sup>, whose Pt NPs are much smaller than those in Pt/MO<sub>2-x</sub>.

The ORR polarization curves of Pt/MO<sub>2-x</sub> catalysts are shown in [Fig. 8b and c](#). The half wave potential (E<sub>1/2</sub>) and onset potential (E<sub>onset</sub>) of Pt/MO<sub>2-x</sub> catalysts are higher than those of Pt/C catalyst (0.853 V, 0.921 V). Pt/T-raw with insignificant amount of oxygen defect also shows higher E<sub>1/2</sub> (0.875 V) and E<sub>onset</sub> (0.927 V), suggestive of SMSI effect. The magnitudes of up-shifts of the two potentials increase as the amount of defect increases, reaching the maximum values of 0.898 and 0.956 V for Pt/T370 catalyst and then are slightly decreased in Pt/T400 with 0.893 and 0.945 V. Likewise, all the catalysts using ZrO<sub>2</sub> and ZrO<sub>2-x</sub> as supports show increased E<sub>1/2</sub> and E<sub>onset</sub> from those of Pt/C, and the magnitudes of upshifts increase with the heat-treatment temperature reaching the highest values of 0.904 and 0.953 V for Pt/Z438.

The Tafel plots in [Figs. 8c and 9c](#) also show that the Pt/MO<sub>2-x</sub> catalysts have much higher electron transfer kinetics from the catalytic sites to bound oxygen atoms than the reference Pt/C catalyst and that the enhancement increases in the order observed in E<sub>1/2</sub> and E<sub>onset</sub> values. That is, among the Pt/TiO<sub>2-x</sub> catalysts, Pt/T370 shows the lowest Tafel slope of 61 mV dec<sup>-1</sup> and among the Pt/ZrO<sub>2-x</sub> catalysts, Pt/Z438 shows the lowest Tafel slope of 54 mV dec<sup>-1</sup>, both of which are much smaller than 84 mV dec<sup>-1</sup> of Pt/C catalyst.

All Pt/MO<sub>2-x</sub> catalysts show considerably enhanced MA and SA from those of Pt/C which shows MA of 0.216 A mg<sub>Pt</sub><sup>-1</sup> and SA of 0.483 mA cm<sup>-2</sup> ([Figs. 8d and 9d](#); numerical data in [Table 1](#)). Even Pt/T-raw (Pt/Z-raw) catalyst with unreduced TiO<sub>2</sub> (ZrO<sub>2</sub>) support shows

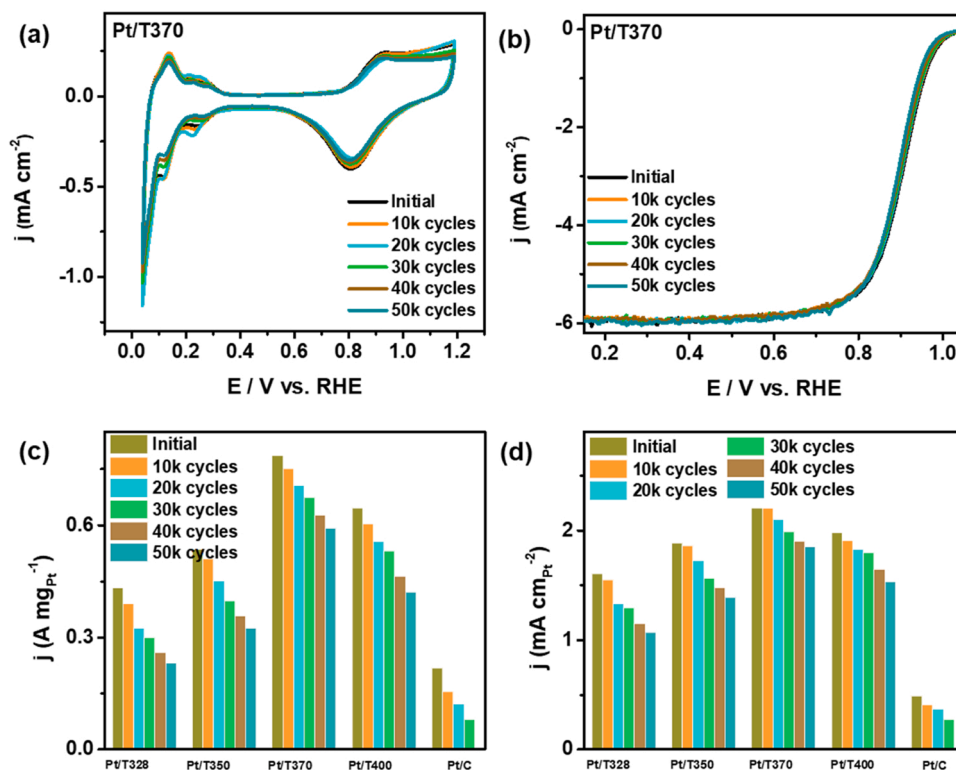


**Fig. 10.** Electrochemical performance of Pt/T370 catalyst before and during (taken after each 10k cycles) 50,000 AST cycles: (a) CV and (b) LSV curves, and plots of (c) normalized mass activity and (d) specific activity at 0.9 V.



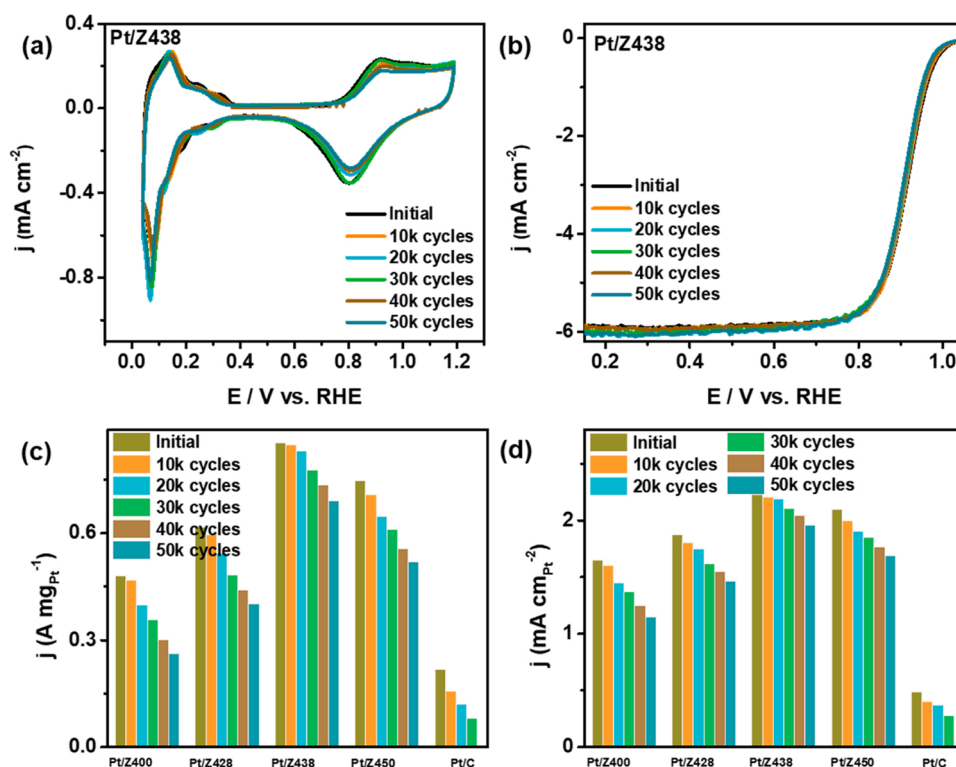


**Fig. 11.** Electrocatalytic performance of Pt/Z438 catalyst before and during (taken after each 10k cycles) 50,000 AST cycles: (a) CV and (b) LSV curves, and plots of (c) normalized mass activity and (d) specific activity at 0.9 V.

enhanced MA of 0.277 (0.319)  $\text{A mg}_{\text{Pt}}^{-1}$  and SA of 1.122 (1.142)  $\text{mA cm}^{-2}$ . Of the catalysts with reduced  $\text{MO}_{2-x}$  supports, MA and SA show the general trend of increase as the heat-treatment temperature increases except for the overturns between Pt/T370 and Pt/T400 and between Pt/Z438 and Pt/Z450. Therefore, the highest activity is found in Pt/T370 (Pt/Z438) with MA of 0.786 (0.852)  $\text{A mg}_{\text{Pt}}^{-1}$  and SA of 2.201 (2.213)  $\text{mA cm}^{-2}$  among the Pt/ $\text{TiO}_{2-x}$  (Pt/ $\text{ZrO}_{2-x}$ ) catalysts, which are 3.64- (3.94-) and 4.56- (4.58-) times enhancements, respectively, from those of Pt/C catalyst.

These large enhancements of electrocatalysis by using  $\text{MO}_{2-x}$  supports over C support can be explained by (a) the SMSI effects seen in the XPS data and (b) the bifunctional mechanism enabled by the  $\text{MO}_{2-x}$  supports with surface -OH groups which C support cannot [64,65]. In addition, to see that the conductivity trend of  $\text{MO}_{2-x}$  support agrees well with the trends of MA and SA in each Pt/ $\text{MO}_{2-x}$  series, the conductivity also seems to affect the overall performance of the catalysts.

### 3.4. The durability of Pt/ $\text{MO}_{2-x}$ catalysts

It is well known that the presently widely used Pt/C catalysts suffer from low stability, caused by the detachment of Pt NPs and their aggregation or growth in size via Oswald ripening. The inherent weakness of C under the strongly acidic and oxidative operating condition is considered to be the major reason for the poor durability [66,67]. The CV curves and LSV curves of Pt/T370 (Pt/Z438) catalyst before and after 50,000 chronoamperometry cycles of the AST protocol are shown in Fig. 10a (Fig. 11a) and 10b (11b), respectively. The loss of ECSA is 10 (9) % for Pt/T370 (Pt/Z438) catalyst after the cycles, much smaller than the ECSA loss of 35% for Pt/C catalyst after, much fewer, 30,000 cycles (Figs. S21–S23, Table S8). Small decreases in  $E_{1/2}$  and  $E_{\text{onset}}$  are observed in Pt/T370 (10 mV, 10 mV) and Pt/Z438 (8 mV, 8 mV) catalysts after the 50,000 cycles, much smaller than the decreases of 44 mV and 43 mV for Pt/C catalyst after 30,000 cycles. Subsequently, the MA and SA of Pt/T370 (Pt/Z438) after 50,000 cycles are 75 (81) % and 84

(88) % of the initial values, respectively, again much higher than 36% for MA and 56% for SA of Pt/C catalyst after 30,000 cycles. Although not as good as Pt/T370 and Pt/Z438, other Pt/ $\text{MO}_{2-x}$  catalysts also show considerably higher stability data than Pt/C catalyst (Table S8).

To understand the origin of the high durability of Pt/ $\text{MO}_{2-x}$  catalysts, we performed TEM studies on them after 50,000 cycles and Pt/C catalyst after 30,000 cycles. While the Pt NPs in Pt/C catalyst after durability test show much larger size (7.0 nm) than the initial size (3.7 nm) (Fig. S24), those in Pt/ $\text{MO}_{2-x}$  catalysts are grown by about ~1 nm from the initial values (Figs. S25–S28). These results clearly demonstrate that the superiority of  $\text{MO}_{2-x}$  substrates in preserving Pt NPs on them during the chronoamperometry cycles. We also performed AST cycles to study the durability of the support materials. After 50,000 AST cycles, the Ti 2p XPS of Pt/T370 and Zr 3d XPS of Pt/Z438 (Fig. S29a, b) show very small peak shifts (0.02 – 0.03 eV) to higher binding energies, which suggests small amounts of reoxidation M in  $\text{MO}_{2-x}$  supports. In contrast, the Pt 4f XPS of these samples (Fig. S29c, d) show no change at all in the binding energy, indicating that the electronic state of Pt in Pt/ $\text{MO}_{2-x}$  catalysts does not change during AST. As to how the electronic state of Pt is unchanged while M in  $\text{MO}_{2-x}$  is oxidized after AST, we propose the following explanation: While some parts of  $\text{MO}_{2-x}$  surface form interfaces with Pt NPs, the other parts do not. The M atoms outside the interfaces are exposed and are prone to the re-oxidation during AST. In contrast, the M atoms in the interfacial parts are protected from the re-oxidation by the reductive potential of Pt. In this explanation, even though a fraction of M may be re-oxidized, its effect is indirect to the Pt- $\text{MO}_{2-x}$  interface, which may be another reason for the enhanced durability of our Pt/ $\text{MO}_{2-x}$  catalysts.

### 3.5. The MEA performance of Pt/ $\text{MO}_{2-x}$ catalysts

We have performed the  $\text{H}_2$ -air single cell measurements for the performance and durability (by running 30,000 AST cycles) of Pt/T370, Pt/Z438 and Pt/C catalysts. Consistent with the half-cell test data, the

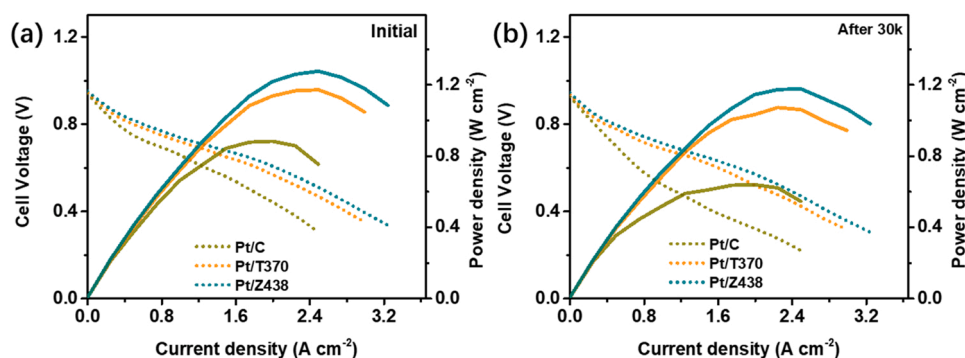


Fig. 12.  $\text{H}_2$ -air fuel cell polarization curve and power density curve on Pt/T370, Pt/Z438 and Pt/C catalysts (a) before and (b) after 30,000 cycles.

MEA polarization and power density data in  $\text{H}_2$ -air cell at  $80^\circ\text{C}$  and ambient pressure (Fig. 12) show that Pt/T370 and Pt/Z438 catalysts outperform Pt/C catalyst by a large margin. The peak power densities are  $1.17$  and  $1.27\text{ W cm}^{-2}$  for Pt/T370 and Pt/Z438 catalysts, respectively, much higher than  $0.89\text{ W cm}^{-2}$  for Pt/C catalyst. The MEA durability was estimated by comparing the performance data after 30,000 cycles under the AST condition with the initial ones. The PEMFCs with Pt/T370 and Pt/Z438 catalysts show performance degradation by 15% and 12%, respectively, in max power density, which are much smaller than 31% performance degradation of Pt/C.

#### 4. Conclusions

In this study, we have achieved high activity and extremely high durability ORR catalysts by depositing Pt NPs on conductive  $\text{MO}_{2-x}$  ( $M = \text{Ti}$  and  $\text{Zr}$ ) supports. The conductive supports were synthesized by solid-state reduction reactions of  $\text{MO}_2$  with  $\text{NaBH}_4$  at high temperatures. By systematically varying the reaction temperature, the optimal temperatures were located to be  $370^\circ\text{C}$  for  $\text{TiO}_2$  and  $438^\circ\text{C}$  for  $\text{ZrO}_2$ , based on the electrical conductivity and ORR performance data. The reduced  $\text{MO}_2$  samples show amorphous regions on the surfaces of the particles in their HRTEM images, which are attributed to the disruption of the lattices induced by the oxygen vacancies. XPS data show a large fraction  $\text{M}^{4+}$  ions are reduced to  $\text{M}^{3+}$  ions whose proportion increases with the heat-treatment temperature. XPS data also show that the electronic structure of Pt is significantly affected by the presence of  $\text{MO}_{2-x}$  supports. Especially, there is a large down-shift of the d-band center of Pt, evidenced by the large down-shifts of  $1.2$ – $1.3\text{ eV}$  compared with that of Pt/C, which probably is one of the largest d-band center-lowering without any other modification on Pt NPs such as doping or shape-controlling. The electrocatalytic data for ORR of Pt/ $\text{MO}_{2-x}$  catalysts show large enhancement of MA and SA from Pt/C catalyst. The significantly enhanced ORR performance of Pt/ $\text{MO}_{2-x}$  catalysts is attributed to the SMSI effect between  $\text{MO}_{2-x}$  and Pt NPs plus bifunctional mechanism from the  $\text{MO}_{2-x}$  surface around Pt NPs. More importantly, Pt/ $\text{MO}_{2-x}$  catalysts exhibit a superior long-term durability. After 50,000 cycles of durability test, Pt/ $\text{TiO}_{2-x}$  370 catalyst retains 75%/84% of initial MA/SA and Pt/ $\text{ZrO}_{2-x}$  438 catalyst 81%/88% of initial MA/SA, while Pt/C keeps only 36%/56% of initial MA/SA after 30,000 cycles. These data surpass the 2025 DOE target of the loss of MA by less than 40% by large margins. TEM images of Pt/ $\text{MO}_{2-x}$  catalysts after the durability tests show practically unchanged shape and size of Pt NPs from those of the as-prepared ones, a sharp contrast to the large Pt NPs in Pt/C catalyst after the durability test. Based on these results, we conclude that the strong Pt- $\text{MO}_{2-x}$  interaction not only modifies the electronic structure of Pt NPs but also stabilizes them under harsh condition of ORR. We believe that there are many possibilities for further improvement of our results by improving the synthesis conditions of  $\text{MO}_{2-x}$  and by investigating other candidate metal oxides for the same goal.

#### CRediT authorship contribution statement

**Wenjuan Shi:** Conceptualization, Methodology, Validation, Formal analysis, Writing – original draft. **Hyun-Uk Park:** Formal analysis, Visualization, Investigation, Validation. **Ah-Hyeon Park:** Visualization, Investigation. **Liangyao Xue:** Visualization, Investigation. **Gu-Gon Park:** Visualization, Investigation. **Seong-Kyu Kim:** DFT calculation. **Young-Uk Kwon:** Methodology, Validation, Supervision, Writing – review & editing.

#### Declaration of Competing Interest

The authors declare that they have no known competing financial interests or personal relationships that could have appeared to influence the work reported in this paper.

#### Data availability

Data will be made available on request.

#### Acknowledgments

This work was supported by Basic Science Research Program through the National Research Foundation of Korea (NRF-2019R1F1A1059485). We appreciate professor Graeme Henkelman of The University of Texas at Austin, USA, for allowing SKK to use the computer facilities to carry out the DFT part of this work.

#### Appendix A. Supplementary material

Supplementary data associated with this article can be found in the online version at [doi:10.1016/j.apcatb.2023.122692](https://doi.org/10.1016/j.apcatb.2023.122692).

#### References

- [1] A. Kulkarni, S. Siahrostami, A. Patel, J.K. Nørskov, Understanding catalytic activity trends in the oxygen reduction reaction, *Chem. Rev.* 118 (2018) 2302–2312.
- [2] M. Shao, Q. Chang, J.P. Dodelet, R.J. Chenitz, Recent advances in electrocatalysts for oxygen reduction reaction, *Chem. Rev.* 116 (2016) 3594–3657.
- [3] Y. Nie, L. Li, Z.J. Wei, Recent advancements in Pt and Pt-free catalysts for oxygen reduction reaction, *Chem. Soc. Rev.* 44 (2015) 2168–2201.
- [4] S. Zhao, T. Liu, Y. Dai, J. Wang, Y. Wang, Z. Guo, J. Yu, I.T. Bello, M.J. Ni, Pt/C as a bifunctional ORR/iodide oxidation reaction (IOR) catalyst for Zn-air batteries with unprecedentedly high energy efficiency of 76.5%, *Appl. Catal. B Environ.* 320 (2023), 121992.
- [5] C. Park, E. Lee, G. Lee, Y.J. Tak, Superior durability and stability of Pt electrocatalyst on N-doped graphene- $\text{TiO}_2$  hybrid material for oxygen reduction reaction and polymer electrolyte membrane fuel cells, *Appl. Catal. B Environ.* 268 (2020), 118414.
- [6] G. Lee, H. Choi, Y.J. Tak, In situ durability of various carbon supports against carbon corrosion during fuel starvation in a PEM fuel cell cathode, *Nanotechnol* 30 (2018), 085402.
- [7] S.Y. Huang, P. Ganesan, S. Park, B.N. Popov, Development of a titanium dioxide-supported platinum catalyst with ultrahigh stability for polymer

- electrolyte membrane fuel cell applications, *J. Am. Chem. Soc.* 131 (2009) 13898–13899.
- [8] F. Ando, T. Gunji, T. Tanabe, I. Fukano, H.D. Abruna, J. Wu, T. Ohsaka, F. J. Matsumoto, Enhancement of the oxygen reduction reaction activity of Pt by tuning its d-band center via transition metal oxide support interactions, *ACS Catal.* 11 (2021) 9317–9332.
  - [9] H. Li, S. Kelly, D. Guevarra, Z. Wang, Y. Wang, J.A. Haber, M. Anand, G. Gunasooriya, C.S. Abraham, S.J. Vijay, Analysis of the limitations in the oxygen reduction activity of transition metal oxide surfaces, *Nat. Catal.* 4 (2021) 463–468.
  - [10] W.J. Lee, S. Bera, H. Woo, H.G. Kim, J.H. Back, W. Hong, J.Y. Park, S.J. Oh, S. H. Kwon, In situ engineering of a metal oxide protective layer into Pt/carbon fuel-cell catalysts by atomic layer deposition, *Chem. Mater.* 34 (2022) 5949–5959.
  - [11] N. Tan, Y. Lei, D. Huo, M. Ding, G. Gao, Y. Zhang, S. Yu, R. Yu, H.J. Du, Fabricating Pt/CeO<sub>2</sub>/N-C ternary ORR electrocatalysts with extremely low platinum content and excellent performance, *J. Mater. Sci.* 57 (2022) 538–552.
  - [12] G.Y. Kim, K.R. Yoon, K. Shin, J.W. Jung, G. Henkelman, W.H. Ryu, Black tungsten oxide nanofiber as a robust support for metal catalysts: high catalyst loading for electrochemical oxygen reduction, *Small* 17 (2021) 2103755.
  - [13] Q. Jia, S. Ghoshal, J. Li, W. Liang, G. Meng, H. Che, S. Zhang, Z.F. Ma, S. J. Mukerjee, Metal and metal oxide interactions and their catalytic consequences for oxygen reduction reaction, *J. Am. Chem. Soc.* 139 (2017) 7893–7903.
  - [14] A.B. Suryamas, G.M. Anilkumar, S. Sago, T. Ogi, K.J. Okuyama, Electrosynthetic Pt/SnO<sub>2</sub> nanofibers as an excellent electrocatalysts for hydrogen oxidation reaction with ORR-blocking characteristic, *Catal. Commun.* 33 (2013) 11–14.
  - [15] J.Q. Lv, Z.L. Lang, J.Q. Fu, Q. Lan, R. Liu, H.Y. Zang, Y.G. Li, D.D. Ye, C.J. Streb, Molecular iron oxide clusters boost the oxygen reduction reaction of platinum electrocatalysts at near-neutral pH, *Angew. Chem. Int. Ed.* (2022), e202202650.
  - [16] G. Mirshekari, C.J. Rice, Effects of support particle size and Pt content on catalytic activity and durability of Pt/TiO<sub>2</sub> catalyst for oxygen reduction reaction in proton exchange membrane fuel cells environment, *J. Power Sources* 396 (2018) 606–614.
  - [17] M. Gustavsson, H. Ekström, P. Hanarp, L. Eurenus, G. Lindbergh, E. Olsson, B. J. Kasemo, Thin film Pt/TiO<sub>2</sub> catalysts for the polymer electrolyte fuel cell, *J. Power Sources* 163 (2007) 671–678.
  - [18] M. Manikandan, R. Vedarajan, R. Kodyath, H. Abe, S. Ueda, A. Dakshnamoorthy, N. Rajalakshmi, K.S. Dhathathreyan, G.V. Ramesh, Pt decorated free-standing TiO<sub>2</sub> nanotube arrays: highly active and durable electrocatalyst for oxygen reduction and methanol oxidation reactions, *J. Nanosci. Nanotechnol.* 16 (2016) 8269–8278.
  - [19] C. Wang, Y. Li, C. Zhang, X. Chen, C. Liu, W. Weng, W. Shan, H.J. He, A simple strategy to improve Pd dispersion and enhance Pd/TiO<sub>2</sub> catalytic activity for formaldehyde oxidation: The roles of surface defects, *Appl. Catal. B Environ.* 282 (2021), 119540.
  - [20] B. Zhang, F. Yang, X. Zhang, N. Wu, B. Liu, Y.J. Li, Construction of graphene-wrapped Pd/TiO<sub>2</sub> hollow spheres with enhanced anti-CO poisoning capability toward photoassisted methanol oxidation reaction, *ACS Sustain. Chem. Eng.* 9 (2021) 1352–1360.
  - [21] R. Gao, J. Xu, J. Wang, J. Lim, C. Peng, L. Pan, X. Zhang, H. Yang, J.J. Zou, Pd/Fe<sub>2</sub>O<sub>3</sub> with electronic coupling single-site Pd-Fe pair sites for low-temperature semihydrogenation of alkynes, *J. Am. Chem. Soc.* 144 (2021) 573–581.
  - [22] F. Ando, T. Tanabe, T. Gunji, T. Tsuda, S. Kaneko, T. Takeda, T. Ohsaka, F. J. Matsumoto, Improvement of ORR activity and durability of Pt electrocatalyst nanoparticles anchored on TiO<sub>2</sub>/cup-stacked carbon nanotube in acidic aqueous media, *Electrochim. Acta* (2017) 404–413.
  - [23] Z. Ma, S. Li, L. Wu, L. Song, G. Jiang, Z. Liang, D. Su, Y. Zhu, R.R. Adzic, J.X. Wang, NbO<sub>x</sub> nano-nail with a Pt head embedded in carbon as a highly active and durable oxygen reduction catalyst, *Nano Energy* 69 (2020), 104455.
  - [24] A. Naldoni, M. Altomare, G. Zoppellaro, N. Liu, S. Kment, R. Zboril, P.J. Schmutki, Photocatalysis with reduced TiO<sub>2</sub>: from black TiO<sub>2</sub> to cocatalyst-free hydrogen production, *ACS Catal.* 9 (2018) 345–364.
  - [25] J. Tian, X. Hu, H. Yang, Y. Zhou, H. Cui, H.J. Liu, High yield production of reduced TiO<sub>2</sub> with enhanced photocatalytic activity, *Appl. Surf. Sci.* 360 (2016) 738–743.
  - [26] M. He, J. Ji, B. Liu, H.J. Huang, Reduced TiO<sub>2</sub> with tunable oxygen vacancies for catalytic oxidation of formaldehyde at room temperature, *Appl. Surf. Sci.* 473 (2019) 934–942.
  - [27] Y. Cui, Q. Ma, X. Deng, Q. Meng, X. Cheng, M. Xie, X. Li, Q. Cheng, H.J. Liu, Fabrication of Ag–Ag<sub>2</sub>O/reduced TiO<sub>2</sub> nanophotocatalyst and its enhanced visible light driven photocatalytic performance for degradation of diclofenac solution, *Appl. Catal. B Environ.* 206 (2017) 136–145.
  - [28] Y. Kim, H.M. Hwang, L. Wang, I. Kim, Y. Yoon, H.J. Lee, Solar-light photocatalytic disinfection using crystalline/amorphous low energy bandgap reduced TiO<sub>2</sub>, *Sci. Rep.* 6 (2016) 1–10.
  - [29] Z. Li, Y. Ding, W. Kang, C. Li, D. Lin, X. Wang, Z. Chen, M. Wu, D.J. Pan, Reduction mechanism and capacitive properties of highly electrochemically reduced TiO<sub>2</sub> nanotube arrays, *Electrochim. Acta* 161 (2015) 40–47.
  - [30] X. Chang, S.S. Thind, A.J. Chen, Electrochemical enhancement of salicylic acid oxidation at electrochemically reduced TiO<sub>2</sub> nanotubes, *ACS Catal.* 4 (2014) 2616–2622.
  - [31] B. Chen, X. Chen, R. Li, W. Fan, F. Wang, B. Mao, W.J. Shi, Flame reduced TiO<sub>2</sub> nanorod arrays with Ag nanoparticle decoration for efficient solar water splitting, *Ind. Eng. Chem. Res.* 58 (2019) 4818–4827.
  - [32] X. Cheng, Q. Cheng, X. Deng, P. Wang, H.J. Liu, A facile and novel strategy to synthesize reduced TiO<sub>2</sub> nanotubes photoelectrode for photoelectrocatalytic degradation of diclofenac, *Chemosphere* 144 (2016) 888–894.
  - [33] M. Nie, H. Sun, J. Liao, Q. Li, Z. Xue, F. Xue, F. Liu, M. Wu, T. Gao, L.J. Teng, Study on the catalytic performance of Pd/TiO<sub>2</sub> electrocatalyst for hydrogen evolution reaction, *Int. J. Hydrog. Energy* 46 (2021) 6441–6447.
  - [34] X. Zhu, J. Li, M. Liu, S.Y. Zhang, X.S. Li, C. Shi, A.M. Zhu, Mesoporous TiO<sub>2</sub> electrocatalysts synthesized by gliding arc plasma for oxygen evolution reaction, *J. Phys. D Appl. Phys.* 54 (2021), 484003.
  - [35] Z. Li, S. Wang, J. Wu, W.J. Zhou, Recent progress in defective TiO<sub>2</sub> photocatalysts for energy and environmental applications, *Renew. Sustain. Energy Rev.* 156 (2022), 111980.
  - [36] C. Foo, Y. Li, K. Lebedev, T. Chen, S. Day, C. Tang, S.C. Tsang, Characterisation of oxygen defects and nitrogen impurities in TiO<sub>2</sub> photocatalysts using variable-temperature X-ray powder diffraction, *Nat. Commun.* 12 (2021) 1–13.
  - [37] C. Cheng, W.H. Fang, R. Long, O.V. Prezhdo, Water splitting with a single-atom Cu/TiO<sub>2</sub> photocatalyst: atomistic origin of high efficiency and proposed enhancement by spin selection, *JACS Au* 1 (2021) 550–559.
  - [38] M. Cadatal-Raduban, J. Pope, J. Olejník, M. Kohout, J.A. Harrison, S.R. Hasan, Ultraviolet-C photoresponsivity using fabricated TiO<sub>2</sub> thin films and transimpedance-amplifier-based test setup, *Sensors* 22 (2022) 8176.
  - [39] S. De la Torre Pari, J. Aquino, A. Carlos-Chilo, J. Guerra, J.A. Coaquira, D. Pacheco-Salazar, J.F. Felix, J. Solis, F.J. Aragón, Enhancing the photoconductivity and gas sensing performance of TiO<sub>2</sub>/SnO<sub>2</sub> heterostructures tuned by the thickness of the SnO<sub>2</sub> upper layer, *Appl. Surf. Sci.* (2022), 156028.
  - [40] A. Nikolaev, A. Suzdaltsev, O. Pavlenko, Y. Zaikov, T. Kurenykh, V.J. Vykhodets, Reduction of ZnO during SNF pyrochemical reprocessing, *J. Electrochem. Soc.* 168 (2021), 036506.
  - [41] D. Zu, H. Wang, T. Yang, H. Wei, S. Sun, H.J. Wu, Black ZnO synthesized by molten lithium reduction strategy for photocatalytic hydrogen generation, *J. Am. Ceram. Soc.* 103 (2020) 4035–4042.
  - [42] Q. Wang, K. Edalati, Y. Koganemaru, S. Nakamura, M. Watanabe, T. Ishihara, Z. J. Horita, Photocatalytic hydrogen generation on low-bandgap black zirconia (ZrO<sub>2</sub>) produced by high-pressure torsion, *J. Mater. Chem. A* 8 (2020) 3643–3650.
  - [43] Y. Li, C. Zhang, J. Ma, M. Chen, H. Deng, H.J. He, High temperature reduction dramatically promotes Pd/TiO<sub>2</sub> catalyst for ambient formaldehyde oxidation, *Appl. Catal. B Environ.* 217 (2017) 560–569.
  - [44] K.M. Naik, T. Hamada, E. Higuchi, H.J. Inoue, Defect-rich black titanium dioxide nanosheet-supported palladium nanoparticle electrocatalyst for oxygen reduction and glycerol oxidation reactions in alkaline medium, *ACS Appl. Energy Mater.* 4 (2021) 12391–12402.
  - [45] Y.H. Qin, Y. Li, T. Lam, Y.J. Xing, Nitrogen-doped carbon–TiO<sub>2</sub> composite as support of Pd electrocatalyst for formic acid oxidation, *J. Power Sources* 284 (2015) 186–193.
  - [46] P.S. Kumar, V.K. Ponnusamy, K.R. Deepthi, G. Kumar, A. Pugazhendhi, H. Abe, S. Thirupuranthagan, U. Pal, S.K. Krishnan, Controlled synthesis of Pt nanoparticle supported TiO<sub>2</sub> nanorods as efficient and stable electrocatalysts for the oxygen reduction reaction, *J. Mater. Chem. A* 6 (2018) 23435–23444.
  - [47] B. Pitna Laskova, L. Kavan, M. Zukalova, K. Moeck, O.J. Frank, In situ Raman spectroelectrochemistry as a useful tool for detection of TiO<sub>2</sub> (anatase) impurities in TiO<sub>2</sub> (B) and TiO<sub>2</sub> (rutile), *Mon. Chem.* 147 (2016) 951–959.
  - [48] A. Shirpay, M.J. Tavakoli, The behavior of the active modes of the anatase phase of TiO<sub>2</sub> at high temperatures by Raman scattering spectroscopy, *Indian J. Phys.* 96 (2022) 1673–1681.
  - [49] S.A. Abdullah, M.Z. Sahdan, N. Nayan, Z. Embong, C.R. Hak, F.J. Adriyanto, Neutron beam interaction with rutile TiO<sub>2</sub> single crystal (1 1 1): Raman and XPS study on Ti<sup>3+</sup>-oxygen vacancy formation, *Mater. Lett.* 263 (2020), 127143.
  - [50] X. Xue, W. Ji, Z. Mao, H. Mao, Y. Wang, X. Wang, W. Ruan, B. Zhao, J.R. Lombardi, Raman investigation of nanosized TiO<sub>2</sub>: effect of crystallite size and quantum confinement, *J. Phys. Chem. C* 116 (2012) 8792–8797.
  - [51] Y.J. Wu, J. Yang, T.X. Tu, W.Q. Li, P.F. Zhang, Y. Zhou, J.F. Li, J.T. Li, S.G. Sun, Evolution of cationic vacancy defects: a motif for surface restructuring of OER precatalyst, *Angew. Chem. Int. Ed.* 60 (2021) 26829–26836.
  - [52] Z. Wang, J. Xu, J. Yang, Y. Xue, L.J. Dai, Ultraviolet/ozone treatment for boosting OER activity of MOF nanoneedle arrays, *J. Chem. Eng.* 427 (2022), 131498.
  - [53] J. Zhou, Z. Han, X. Wang, H. Gai, Z. Chen, T. Guo, X. Hou, L. Xu, X. Hu, M. J. Huang, Discovery of quantitative electronic structure–OER Activity relationship in metal–organic framework electrocatalysts using an integrated theoretical-experimental approach, *Adv. Funct. Mater.* 31 (2021) 2102066.
  - [54] Y. Yan, C. Liu, H. Jian, X. Cheng, T. Hu, D. Wang, L. Shang, G. Chen, P. Schaaf, X. J. Wang, Substitutionally dispersed high-oxidation CoO<sub>x</sub> clusters in the lattice of rutile TiO<sub>2</sub> triggering efficient Co–Ti cooperative catalytic centers for oxygen evolution reactions, *Adv. Funct. Mater.* 31 (2021) 2009610.
  - [55] Y. Wang, R. Zhang, J. Chen, H. Wu, S. Lu, K. Wang, H. Li, C.J. Harris, K. Xi, R. V. Kumar, Enhancing catalytic activity of titanium oxide in lithium–sulfur batteries by band engineering, *Adv. Energy Mater.* 9 (2019) 1900953.
  - [56] Z. Fohlerova, K. Kamnev, M. Sepúlveda, Z. Pytlíček, J. Prasek, A.J. Mozalev, Nanostructured zirconium-oxide bioceramic coatings derived from the anodized Al/Zr metal layers, *Adv. Mater. Interfaces* 8 (2021) 2100256.
  - [57] X. Liu, Y. Ren, M. Wang, X. Ren, J. Liu, Q.J. Yang, Cooperation of Pt and TiO<sub>x</sub> in the hydrogenation of nitrobenzothiazole, *ACS Catal.* 12 (2022) 11369–11379.
  - [58] J.Z. Chen, A. Talpade, G.A. Canning, P.R. Probus, F.H. Ribeiro, A.K. Datye, J. T. Miller, Strong metal–support interaction (SMSI) of Pt/CeO<sub>2</sub> and its effect on propane dehydrogenation, *Catal. Today* 371 (2021) 4–10.
  - [59] R. Huang, O. Kwon, C. Lin, R.J. Gorte, The effects of SMSI on m-Cresol hydrodeoxygenation over Pt/Nb<sub>2</sub>O<sub>5</sub> and Pt/TiO<sub>2</sub>, *J. Catal.* 398 (2021) 102–108.
  - [60] Z. Chen, L. Liang, H. Yuan, H. Liu, P. Wu, M. Fu, J. Wu, P. Chen, Y. Qiu, D.J. Ye, Reciprocal regulation between support defects and strong metal–support interactions for highly efficient reverse water gas shift reaction over Pt/TiO<sub>2</sub> nanosheets catalysts, *Appl. Catal. B Environ.* 298 (2021), 120507.

- [61] M. Smiljanić, S. Panić, M. Bele, F. Ruiz-Zepeda, L. Pavko, L. Gašparić, A. Kokalj, M. Gaberšček, N.J. Hodnik, Improving the HER activity and stability of Pt nanoparticles by titanium oxynitride support, *ACS Catal.* (2022) 13021–13033.
- [62] J. Chen, G. Qian, B. Chu, Z. Jiang, K. Tan, L. Luo, B. Li, S.J. Yin, Tuning d-band center of Pt by PtCo–PtSn heterostructure for enhanced oxygen reduction reaction performance, *Small* 18 (2022) 2106773.
- [63] X. Qi, T. Yang, P. Li, Z.J. Wei, DFT study on ORR catalyzed by bimetallic Pt–skin metals over substrates of Ir, Pd and Au, *Nano Mater. Sci.* (2021).
- [64] M. Wang, Z. Wang, S. Hu, X. Zhu, X. Lin, X. Zhang, P.K. Shen, A facile strategy synthesized PtRhNi truncated triangle nanoflakes with PtRh-rich surface as highly active and stable bifunctional catalysts for direct methanol fuel cells, *J. Colloid Interface Sci.* 604 (2021) 894–902.
- [65] T. Xia, K. Zhao, Y. Zhu, X. Bai, H. Gao, Z. Wang, Y. Gong, M. Feng, S. Li, Q.J. Zheng, Mixed-dimensional Pt–Ni alloy polyhedral nanochains as bifunctional electrocatalysts for direct methanol fuel cells, *Adv. Mater.* (2022) 2206508.
- [66] D. Liu, J. Zhang, D. Liu, T. Li, Y. Yan, X. Wei, Y. Yang, S. Yan, Z.J. Zou, N-doped graphene-coated commercial Pt/C catalysts toward high-stability and antipoisoning in oxygen reduction reaction, *J. Phys. Chem. Lett.* 13 (2022) 2019–2026.
- [67] R. Xu, L. Kang, K.G. Papanikolaou, B. Wang, S. Marlow, Q. He, P. Zhang, J. Wang, D.J. Brett, M.J. Stamatakis, Improving the ORR performance by enhancing the Pt oxidation resistance, *J. Catal.* 416 (2022) 311–321.